An Efficient Predictive Current Control Strategy for a Four-Level Open-End Winding Induction Motor Drive

Suresh Lakhimsetty, *Member, IEEE*, and V. T. Somasekhar, *Member, IEEE*

***Abstract*—This article proposes a new predictive current control (PCC) strategy for a dual-inverter fed four-level (4-L) open-end winding induction motor drive (OEWIMD). The individual inverters of the dual-inverter system are operated with dc-link voltages, which are in the ratio of 2:1. In general, the PCC for the 4-L OEWIMD requires the evaluation of all of the 37 available voltage vectors (VVs) to select the optimal one. An improvised PCC is proposed in this article, wherein the inverter with lower dc-input voltage is clamped, while the other inverter is switched around it. An important feature of the proposed PCC is that it evaluates only five candidate VVs to determine the optimal vector. The simulation and the experimental results reveal that the performance of the proposed PCC technique is superior to the conventional PCC in terms of voltage and current total harmonic distortion (THD), torque-ripple, and total drive loss. Furthermore, the proposed PCC results in the reduction of the computational burden on the controller. Also, as the reduction of switching frequency is inherent in the proposed PCC strategy, there is no requirement to add an additional constraint to reduce it in the cost function.**

***Index Terms*—AC motor drives, NSHC, open-end winding induction motor drive, predictive control, pulsewidth-modulated inverters, torque control.**

I. Introduction

FINITE-SET model predictive control (FS-MPC) techniques are extensively being researched in the area of power electronics and motor drive applications [1]–[3]. The availability of fast control platforms, which can cope with extensive computational burden, is the principal contributing factor for the application of FS-MPC to electric drive applications. The advantages of the FS-MPC technique include simplicity of implementation, quick response, multivariable control, and the ability to handle more nonlinear constraints [4]–[8]. In spite of these positive features, the FS-MPC suffers from drawbacks such as: dependence on the model parameters of the system, increased number of prediction horizons to avoid calculation delay, complicated estimation of unmeasurable state components, and variable switching frequency [4]–[8]. Though some of the aforementioned problems are solved [9], [10], the tuning of weighting factor is still a very challenging task in the implementation of FS-MPC, especially when the control variables have different amplitudes and units.

When the FS-MPC is aimed to control the torque and flux of an induction motor (IM), it is named as predictive torque control (PTC), which is an alternative to direct torque control (DTC) [11]. Instead of choosing the voltage vector (VV) from a predefined look-up table, PTC selects an optimal VV to control the errors in flux and torque of an IM drive.

Recently, the field-oriented control (FOC) technique was implemented by using FS-MPC algorithm, named as predictive FOC or predictive current control (PCC) and applied on voltage source inverter (VSI) with *RL* load [4]. This is an alternative to PTC to control electrical drives. Instead of minimizing the errors in torque and flux magnitudes as in PTC, PCC directly exerts control over the motor phase currents, without any weighting factor in its cost function. This makes the algorithm very simple and less burdensome to the processor, without sacrificing the transient and steady-state performances of motor drives [12]. Thus, theoretically, the implementation of PCC is easier than PTC. This fact motivates researchers to apply this technique to power electronics [1], [4], [12] and other applications [13].

A common problem encountered while implementing the PCC is the computational burden posed on the control platform and the choice of predictive horizon. In [8], it is shown that the drive performance deteriorates if the predictive horizon is chosen as *one*. Instead, if the predictive horizon is chosen as *two*, the drive performance is improved [8]. It is known that FS-MPC-based control strategies always choose the optimal VV in a sampling period among the available VVs, which causes variable switching frequency [6].

The work reported in [12] addresses the issue of variable switching frequency by adding a switching frequency control term to the cost function of the PCC technique.

FS-MPC for various applications with extended discontinuous modulation schemes are reported in [14] and [15] to reduce the switching frequency. However, because of these additional constraints, the calculating time for the cost function increases.

A sensorless IM drive is proposed in [16], which is based on the stator-flux-oriented control. In this article, the linear PI controllers are replaced with PCC.

Linear and nonlinear MPC techniques, based on the current control or flux/torque control, are extended for three-level open-end winding induction motor drives (OEWIMD) with common dc-link voltage [17]. In this article, the cost function minimizes

Manuscript received February 27, 2019; revised June 18, 2019 and September 23, 2019; accepted November 11, 2019. Date of publication November 20, 2019; date of current version February 20, 2020. Recommended for publication by Associate Editor Dr. H. Hofmann. *(Corresponding author: Suresh Lakhimsetty.)*

S. Lakhimsetty is with the Department of Electrical and Electronics Engineering, V R Siddhartha Engineering College, Vijayawada 520007, India (e-mail: suresh.201@gmail.com).

V. T. Somasekhar is with the Department of Electrical Engineering, National Institute of Technology Warangal, Warangal 506004, India (e-mail: sekhar@nitw.ac.in).

Color versions of one or more of the figures in this article are available online at http://ieeexplore.ieee.org.

Digital Object Identifier 10.1109/TPEL.2019.2954864

the stator current error along with the zero-sequence current as in the case of nonlinear PCC.

The work reported in [18] presents the direct flux-vector control of IM drives. The proposed method combines the advantages of both DTC and the fast current-vector control. However, the difficulty associated with the tuning of the flux weighting factor in the cost function could not be avoided in this article.

A double-vector-based predictive hysteresis current controller is proposed for a two-level inverter fed IM to improve its steady-state performance [19]. The proposed technique uses one active vector and one null vector. However, the advantage gets weak as the motor speed increases.

The work reported in [20] presents a multistep MPC technique for medium voltage drives to reduce the stator current harmonics and to improve the drive performance. However, it uses a frequency term in its cost function to reduce the switching power loss. An additional PI controller is also employed in this article to tune the rotor-flux component.

The work proposed in [21] proposes a PCC technique, which achieves an enhanced voltage utilization of the dual-inverter fed OEWIMD. An appropriate weighting factor is added to the floating capacitor voltage term in the cost function to enhance the dc-link utilization by 10%. However, to balance the floating capacitor voltage, the cost function incorporates an additional term. This poses difficulty in tuning the weighting factor.

A new cascaded FS-MPC scheme with reduced computational burden is proposed for a four-level (4-L) OEWIMD [22]. In this scheme, the VVs of the inverter with higher dc-link voltage are obtained under the assumption that the second inverter is in the short-circuited state. While the first inverter is clamped, the switching states of the second inverter (along with the clamped state of the first inverter) are used in the predictive calculations. The proposed technique uses 13 VVs instead of 37. However, the proposed method of selecting VVs could result in the overcharging of the capacitor of the second inverter in the midspeed range of operation [23].

This article proposes an improvised PCC strategy for a 4-L OEWIMD to select the optimal VV. The optimal VV is selected based on the clamping of one of the inverter (operating with lower dc-link voltage) and is identified by using the concept of the nearest subhexagonal center (NSHC). The other inverter is switched around the clamped inverter. The cost function of the proposed scheme takes only five VVs to evaluate the optimal value based on the difference of two VVs, without adding any additional constraints. The proposed PCC improves the performance of the drive in terms of the voltage and current total harmonic distortions (THDs) and ripple in the steady-state torque. It is shown that, except in the midspeed range, the overall power loss in the drive system is reduced with the proposed PCC compared to the conventional PCC. Furthermore, the proposed scheme reduces the switching frequency and the computational burden on the controller.

The behavior of the 4-L OEWIMD with the proposed PCC is assessed with simulation studies. The simulation results are validated with experimental results. The agreement of the simulation and experimental results proves the advantage of the proposed PCC over its conventional counterpart.

II. Comparison of FOC and PCC

In the FOC, the stator current vector is decoupled into two orthogonal components, namely the direct-axis (d-axis) and the quadrature-axis (q-axis) components. The d-axis is aligned to the axis of the rotor flux under all dynamic conditions. The d-axis component of the stator current (usually denoted as i_{ds} in literature) controls the rotor flux, while the q-axis component of the stator current (usually denoted as i_{qs} in literature) controls the torque produced by the machine. As the vectors i_{ds} and i_{qs} are orthogonal to each other, they are essentially noninterfering in nature, a situation similar to the dc motor. Thus, FOC equips an induction motor to emulate the fast dynamic behavior of a dc motor [25]. The implementation FOC typically requires a rotor flux observer (RFO) in order to track the axis of the rotor flux. Besides tracking the axis of the rotor flux, the RFO provides the d- and q-components of the actual stator current vector, which are fed back to the respective proportional integral (PI) controllers, to control them.

The FOC technique is a linear control strategy, which uses linear controllers and the pulsewidth modulator. The outputs of the two current controllers are input to the pulsewidth modulation (PWM) modulator to generate the gating pulses to the power semiconductor switching devices of the VSI, which feeds the induction motor. A typical implementation of FOC requires one speed PI controller and two current PI controllers. This requires the tuning of several parameters making FOC cumbersome to implement.

The PCC technique is an alternative to the FOC scheme. It belongs to the gamut of the MPC scheme, which has become very popular in recent times. Unlike the FOC scheme, the PCC scheme uses only one PI controller (the speed controller). The speed PI controller determines the reference q-axis current, which produces the required torque. The d-axis reference current is kept constant, corresponding to the rated excitation level of the motor (for controlling the speed below the rated value).

The novelty and advantage of PCC lie in the avoidance of the d- and q-axis current PI controllers. Instead of the usual pulsewidth modulator, the PCC technique employs a cost function. The definition of the cost function is very flexible, as it can be formulated at will, to suit the requirements of the drive. It is easy to incorporate several constraints and multiple objectives in the definition of the cost function [6]. The cost function is evaluated in real-time for all of the possible candidate solutions (VVs offered by the dual-inverter system in the present case) and the optimal solution (VV) is chosen.

In PCC, the reference currents (i.e., i^*_{ds} and i^*_{qs}) are predicted based on the sensed quantities (two stator currents and speed) and are compared with the sampled values at the present instant to determine the optimal vector. Based on the optimal vector, the switching combinations are selected and fed to inverters.

To implement FOC or PCC for the three-phase OEWIMD, it is required to sense at least two motor phase currents and the speed of the rotor.

III. Modeling of Four-Level OEWIM Drive

The circuit diagram for the 4-L OEWIM drive is shown in Fig. 1. The dc-link voltages of Fig. 1 are maintained in the ratio of 2:1, to realize 4-L inversion [24] and isolated power supplies are used to avoid the path for the zero-sequence current.

The individual inverters of this OEWIM drive have eight individual switching states, and hence the resultant space vector diagram for the dual-inverter system of the OEWIMD has 64 space vector combinations spread over 37 space vector locations, as shown in Fig. 2.

The mathematical model of an induction motor can be extended to an OEWIM in any arbitrary reference frame rotating

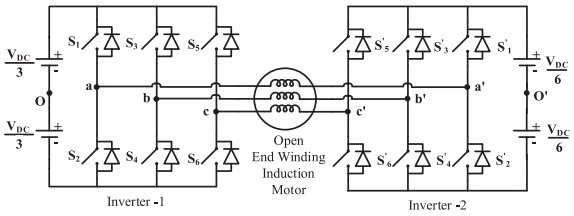

Fig. 1. Circuit diagram of 4-L OEWIM drive.

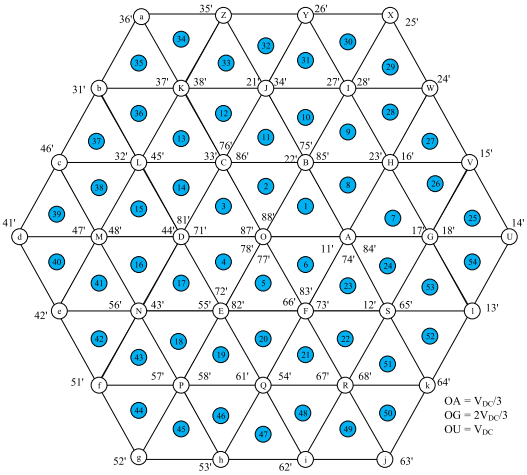

Fig. 2. Dual-inverter system overall space vector diagram.

at an angular frequency of ω_a, which is given by

$$\bar{\nu}_s = R_s \bar{i}_s + d\bar{\psi}_s/dt + j\omega_a \bar{\psi}_s \tag{1}$$

$$\bar{\nu}_r = R_r \bar{i}_r + d\bar{\psi}_r/dt + j\left(\omega_a - \omega\right)\bar{\psi}_r \tag{2}$$

$$\bar{\psi}_s = L_s \bar{i}_s + L_m \bar{i}_r \tag{3}$$

$$\bar{\psi}_r = L_m \bar{i}_s + L_r \bar{i}_r \tag{4}$$

The subscripts *s* and *r* stand for stator and rotor variables, respectively. The symbols $\bar{v}_s$ and $\bar{v}_r$, respectively, denote the space vectors corresponding to the applied stator voltage and the rotor voltage (which is equal to zero, for a squirrel cage machine). Similarly, the symbols $\bar{i}_s$ and $\bar{i}_r$ denote the current vectors, and $\bar{\psi}_s$ and $\bar{\psi}_r$ denote the flux-linkage vectors. R_s and R_r are the resistances, L_s and L_r are the inductances, and L_m is the mutual inductance. The variable ω represents the electrical rotor angular speed. In general, the rotor resistance R_r is referred to the primary side (i.e., stator), which is denoted as R_{rp}.

The pole voltages of inverter-1 $(v_{ao}, v_{bo}, \text{ and } v_{co})$ and inverter-2 $(v_{a'o'}, v_{b'o'}, \text{ and } v_{c'o'})$ in terms of switching pulses are shown as [11]

$$\begin{bmatrix} \nu_{ao} \\ \nu_{bo} \\ \nu_{co} \end{bmatrix} = \frac{2V_{\mathrm{DC}}}{3} \begin{bmatrix} s_{ay} \\ s_{by} \\ s_{cy} \end{bmatrix} \tag{5}$$

$$\begin{bmatrix} \nu_{a'o'} \\ \nu_{b'o'} \\ \nu_{c'o'} \end{bmatrix} = \frac{V_{\mathrm{DC}}}{3} \begin{bmatrix} s_{a'y} \\ s_{b'y} \\ s_{c'y} \end{bmatrix} \tag{6}$$

where

$$s_{xy} = 0,\ 1\ \ (x \in a, b, c, a', b', c' \text{ and } y \in 1, 2, 3, 4, 5, 6)\,.$$

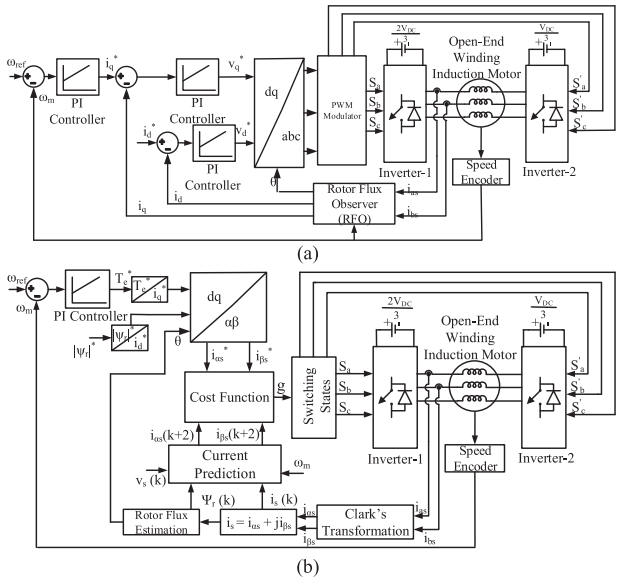

Fig. 3. Block diagrams of the 4-L OEWIMD. (a) Conventional FOC. (b) Conventional PCC.

The voltage across the stator phase winding of OEWIM is the difference between pole voltages of inverter-1 and 2 shown as

$$\begin{bmatrix} \Delta\nu_{aa'} \\ \Delta\nu_{bb'} \\ \Delta\nu_{cc'} \end{bmatrix} = \begin{bmatrix} \nu_{ao} \\ \nu_{bo} \\ \nu_{co} \end{bmatrix} - \begin{bmatrix} \nu_{a'o'} \\ \nu_{b'o'} \\ \nu_{c'o'} \end{bmatrix} \tag{7}$$

Using (7), the zero-sequence voltages are defined as

$$\nu_z = \frac{1}{3}\left[\Delta\nu_{aa'} + \Delta\nu_{bb'} + \Delta\nu_{cc'}\right] \tag{8}$$

From (7) and (8), the phase voltage expressions of the OEWIMD are given as

$$\begin{bmatrix} \nu_{aa'} \\ \nu_{bb'} \\ \nu_{cc'} \end{bmatrix} = \begin{bmatrix} \Delta\nu_{aa'} - \nu_z \\ \Delta\nu_{bb'} - \nu_z \\ \Delta\nu_{cc'} - \nu_z \end{bmatrix} \tag{9}$$

$$\begin{bmatrix} \nu_{aa'} \\ \nu_{bb'} \\ \nu_{cc'} \end{bmatrix} = \frac{1}{3} \begin{bmatrix} 2 & -1 & -1 \\ -1 & 2 & -1 \\ -1 & -1 & 2 \end{bmatrix} \begin{bmatrix} \Delta\nu_{aa'} \\ \Delta\nu_{bb'} \\ \Delta\nu_{cc'} \end{bmatrix} \tag{10}$$

Using (10) and Clark transformation, the quadrature components of the motor phase voltages are given as

$$\nu_{\alpha s} = \frac{3}{2}\,\nu_{aa'} \tag{11}$$

$$\nu_{\beta s} = \frac{\sqrt{3}}{2}\left(\nu_{bb'} - \nu_{cc'}\right) \tag{12}$$

IV. Conventional Predictive Current Controller for a Four-Level OEWIMD

The basic block diagrams of the 4-L OEWIM drive, which employs the conventional FOC and the PCC, are shown in Fig. 3. As mentioned in Section II, the PCC-based drive avoids the *q*-axis and the *d*-axis current controllers, which are essential for the FOC-based drive. From Fig. 3(b), it may be noted that the following quantities need to be measured at the kth sampling instant to implement the PCC.

1) Stator currents for any two phases, say $i_{as}(k)$ and $i_{bs}(k)$, from which, the stator current space vector $\bar{i}_s(k)$ is obtained.
2) The dc-link voltage $\mathrm{V_{dc}}$ and the available dual-inverter system switching states together are used to constitute the stator voltage space vector $\bar{v}_s(k)$.
3) The motor speed $w_m(k)$.

Based on these quantities, the rotor flux vector $\psi_r(k)$ is estimated. Using the Clark's transformation, the measured stator currents $i_{as}(k)$ and $i_{bs}(k)$ are converted into $i_{\alpha s}(k)$ and $i_{\beta s}(k)$ and are compared with the reference currents $i^*_{\alpha s}(k)$ and $i^*_{\beta s}(k)$ respectively. These references (i.e., $i^*_{\alpha s}(k)$ and $i^*_{\beta s}(k)$) are obtained from the speed PI controller and reference rotor flux.

A. Stator Current Prediction

The conventional PCC strategy uses the stator current $(\bar{i}_s)$ and rotor flux $(\bar{\psi}_r)$ as state variables [25]. The stator currents can be directly measured, whereas the rotor flux has to be estimated, because the rotor state variables cannot be measured directly in a squirrel cage machine. From (1)–(4), the estimated value of the rotor flux is given as [6], [25]

$$\bar{\psi}_r + \tau_r \frac{d\bar{\psi}_r}{dt} = -j\left(\omega_a - \omega\right)\tau_r \bar{\psi}_r + L_m \bar{i}_s \tag{13}$$

From the measured currents and the estimated ψ_r, the stator current can be obtained as [6]

$$\bar{i}_s + \tau_\sigma d\bar{i}_s/dt = -j\omega_a \tau_\sigma \bar{i}_s + k_r/R_\sigma\left(1/\tau_r - j\omega\right)\bar{\psi}_r + \bar{\nu}_s/R_\sigma \tag{14}$$

where $T_s = L_s/R_s$, $T_r = L_r/R_{rp}$, $\sigma = 1 - (\frac{((L_m)^2)}{(L_r L_s)})$, $k_r = L_m/L_r$, $R_\sigma = R_s + K_r^2 R_{rp}$, $\tau_\sigma = \sigma L_s/R_\sigma$.

Equation (14) is discretized using the following relationships and considerations:

1) $$\frac{d\bar{i}_s}{dt} = \frac{\bar{i}_s\left(k+1\right) - \bar{i}_s\left(k\right)}{T_s}$$
2) $\omega_a = 0$ (i.e., stationary frame is chosen for prediction and control).
2) The rotor flux $\bar{\psi}_r(k)$ is a constant.
4) The voltage space vector is the optimum vector obtained by the evaluation of the cost function (shown in Fig. 3(b) and discussed in the next section) in the previous (i.e., $(k-1)^{th}$) sampling time period.

Based on the above relationships and considerations, the discretized version of (14) is

$$\bar{i}^p_s\left(k+1\right) = \left(1 + \frac{T_s}{\tau_\sigma}\right)\bar{i}_s\left(k\right) + \frac{T_s}{\tau_\sigma + T_s} \times \left\{\frac{1}{R_\sigma}\left[\left(\frac{k_r}{\tau_r} - k_r j\omega_m\right)\bar{\psi}_r\left(k\right) + \bar{\nu}_s\left(k\right)\right]\right\} \tag{15}$$

Furthermore, the following observations are made based on the implementation issues:

1) Delay due to data acquisition, computation and outputs are inevitable in digital control systems, which must be compensated for.
2) In MPC systems, the optimal vector corresponding to the $(k+1)$th instant should be predicted at the kth instant. This optimal vector must be applied at the kth instant itself.
3) Since it is impossible to achieve this objective (due to the delay), the predictive horizon is extended and the optimal vector corresponding to the $(k+2)$th instant is obtained by applying all of the candidate vectors (37 or 5 in the present case for the 4-L OEWIMD) to the cost function.
4) Since all of this activity takes place between the (k)th and $(k+1)$th instants, the optimal vector (i.e. $\bar{v}_s(k+1)$) applied at the $(k+1)$th instant forces $\bar{i}_s(k+2)$ to become equal to the reference current generated by speed-PI controller and reference rotor flux, i.e.,

$$i^*_\alpha\left(k+2\right) + ji^*_\beta\left(k+2\right) = i_\alpha\left(k+2\right) + ji_\beta\left(k+2\right).$$

Owing to the extension of the predictive horizon to the $(k+2)$th instant, (15) becomes as

$$\bar{i}^p_s\left(k+2\right) = \left(1 + \frac{T_s}{\tau_\sigma}\right)\bar{i}^p_s\left(k+1\right) + \frac{T_s}{\tau_\sigma + T_s}\left\{\frac{1}{R_\sigma} \times \left[\left(\frac{k_r}{\tau_r} - k_r j\omega_m\right)\bar{\psi}_r\left(k+1\right) + \bar{\nu}_s\left(k+1\right)\right]\right\} \tag{16}$$

From (16), it can be observed that the predicted current values are also dependent on the dual-inverter system voltage$(\bar{\nu}_s(k+1))$. As explained earlier, the 4-L OEWIMD possesses a total of 64 space vector combinations spread over 37 space vector locations (Fig. 2). Using (10), (11), and (12), the dual-inverter voltage space vector $(\bar{\nu}_s(k+1))$ is computed in the stationary frame of reference for all of the 37 space vector combinations.

B. Reference Currents Generation

The generation of reference currents is necessary for the predictive current controller. The reference torque component (T^*_e) is the output of the speed PI controller, which tries to make the error between the reference speed and actual speed to zero. The rotor flux reference (ψ^*_r) is a constant, which is equal to the rated rotor flux of the machine. The values of the reference currents (i^*_q, i^*_d) for the respective T^*_e and ψ^*_r in rotor field orientation are calculated as [12]

$$\left.\begin{aligned} i^*_q\left(k\right) &= \tfrac{2}{3}\tfrac{L_r}{L_m}\tfrac{T^*_e}{|\psi^*_r|} \\ i^*_d\left(k\right) &= \tfrac{|\psi^*_r|}{L_m} \end{aligned}\right\} \tag{17}$$

The stator current space vector $(i^*_s(k))$ is constructed using (17) and is transformed to the $\alpha\beta$ frame using the inverse-park transformation before getting substituted into the cost function. As mentioned in the previous section, the stator currents are predicted two samples ahead. However, the reference currents pertain only to the present time instant (i.e., kth sampling time interval). Thus, the reference current is also calculated at two samples ahead by the Lagrange extrapolation method [6] and the resultant expression is given as

$$\bar{i}^*_s\left(k+2\right) = 6\bar{i}^*_s\left(k\right) - 8\bar{i}^*_s\left(k-1\right) + 3\bar{i}^*_s\left(k-2\right) \tag{18}$$

C. Cost Function

From the principle of the PCC, for every sample time period, the predicted stator current from all of the possible voltage space vectors is to be compared by its reference value and then an optimal VV is chosen based on the minimal value of the cost function and is defined as

$$g_i\left(p\right) = \sqrt{\left\{\begin{aligned} &\mathrm{real}\left(\left|\bar{i}^*_s\left(k+2\right) - \left(\bar{i}^p_s\left(k+2\right)_p\right)\right|\right)^2 + \\ &\mathrm{imag}\left(\left|\bar{i}^*_s\left(k+2\right) - \left(\bar{i}^p_s\left(k+2\right)_p\right)\right|\right)^2 \end{aligned}\right\}} \tag{19}$$

Here, $p \in 0, 1, 2, 3, \ldots, 36$ and the cost function evaluates all of the 37 voltage space vectors to identify the optimal one, which minimizes the error.

It is important to note the following points while implementing the conventional PCC. 1) The compensation delay should be considered; otherwise, the motor-drive performance would deteriorate as documented in [6] and [8]. 2) The cost function has to evaluate all of the 37 candidate voltage space vectors. Due to this, not only the computational burden on the controller is increased but also results in variable switching operation.

V. Nearest Subhexagonal-Based Predictive Current Controller for a Four-Level OEWIMD

As mentioned in the earlier section, in order to determine the optimal VV, the cost function has to be evaluated for all of the 37 voltage space vectors. The main advantage of the OEWIMD is that it is very rich in redundancy of switching states. In [26], a discontinuous modulation scheme based on the space vector PWM technique is proposed, wherein one inverter is operated as a clamping inverter and other inverter acts as a switching inverter. The switching states of the clamping inverter are identified based on the principle of the NSHC (explained in the next section), which is extended here to implement the PCC for the OEWIMD. The detailed procedure is explained as follows.

A. Selection of Optimal Voltage Vector

In the conventional PCC, based on the optimal VV, both of the inverters of the OEWIMD are switched. However, it is possible to have one of the inverters of the dual-inverter system clamped and other one switched around it. The clamped state of the inverter is identified by using the NSHC approach [26]. In order to implement this strategy, (15) is rewritten as

$$\bar{\nu}_s(k) = R_\sigma \left\{ \frac{T_s + \tau_\sigma}{T_s} \left(\overline{i_s^p}(k+1) - \left(\frac{T_s + \tau_\sigma}{T_s} \right) \bar{i}_s(k) \right) \right\} - \left(\frac{k_r}{\tau_r} - j k_r \omega_m \right) \overline{\psi_r}(k) \tag{20}$$

In the conventional PCC, the predicted stator current at $(k+1)$th instant has to be equal to the generated reference currents (output of speed PI controller, reference rotor flux) [6], i.e., $\bar{i}_s^p(k+1) = \bar{i}_s^*(k+1)$ and (20) is rewritten (assuming $\psi_r(k+1) = \psi_r(k)$) as

$$\overline{\nu_s^*}(k+1) = R_\sigma \left\{ \frac{T_s + \tau_\sigma}{T_s} \left(\overline{i_s^*}(k+1) - \left(\frac{T_s + \tau_\sigma}{T_s} \right) \bar{i}_s(k) \right) \right\} - \left(\frac{k_r}{\tau_r} - j k_r \omega_m \right) \overline{\psi_r}(k) \tag{21}$$

From (21), the reference VVs are obtained in the $\alpha\beta-$frame. The following steps are used to identify the NSHC and the corresponding available VVs in each sector.

Step-1: Obtaining the instantaneous reference phase voltage variables $v_a^*, v_b^*,$ and v_c^* from the $v_{\alpha s}^*, v_{\beta s}^*$ using the *inverse-Clark transformation.*

Step-2: Determination of the *maximum* of phase voltage values using $v_{\max} = \max[v_a^*, v_b^*, v_c^*, -v_a^*, -v_b^*, -v_c^*]$ [26].

Step-3: Identification of the NSHC based on Step-2. For example, if v_a^* is the maximum phase voltage, then NSHC is A and inverter-2 of the OEWIMD is clamped to the state $4'(-++)$ (see Fig. 4).

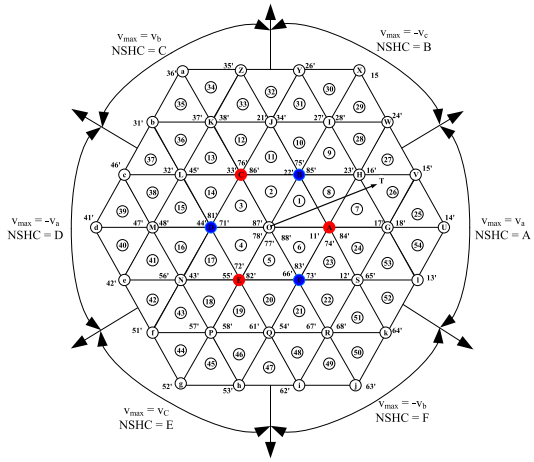

Fig. 4. Voltage vector selection for proposed PCC using NSHC for OEWIMD.

Step-4: Identifying the candidate voltage space vectors based on the NSHC for the switching inverter (inverter-1 in Fig. 1).

Step-5: Identifying the pole phase of the switching inverter, which is clamped to the positive dc-rail or the negative dc-rail, based on the maximum or minimum reference voltages.

To explain the above steps, let it be assumed that $v_{\max} = -v_a^*$ i.e., the NSHC is D (see Fig. 4). Now, inverter-2 of the dual-inverter system acts as the clamped inverter with the sub hexagonal center "D" (i.e., state$1'(+--)$) and the corresponding vector is OD. Inveter-1 acts as the switching inverter. From Fig. 4, the possible space vector switching locations for inverter-1 are at O, D, b, d, and f. From this discussion, it can be concluded that, as compared to the conventional PCC, the VVs are limited to 5 instead of 37. It should be noted that the vectors at O and D are applied in the low-speed range, while the vectors at D, b, d, and f are employed in the medium- and the high-speed range.

Thus, the salient features of the proposed PCC may be enumerated as follows: 1) the identification of NSHC is very simple, and does not require any complicated equations and trigonometric functions. 2) Based on the NSHC, inverter-2 is clamped to one of the six switching states, while inverter-1 is switched around it. In the switching inverter (i.e., inverter-1), one phase is always clamped, depending on the subhexagonal center. For example, in the medium- and high-speed ranges, the vectors employed for the switching inverter, situated at b, d, f, and D, are: $3(-+-)$, $4(-++)$, $5(--+)$, and $8(---)$, respectively. It is obvious that phase-A of inverter-1 is clamped to the negative dc-rail (Fig. 1) when these vectors are switched.

B. Formulation of Cost Function

Sample delay is inevitable in the discrete systems. To accommodate this delay, a compensation scheme is used, wherein the predictive horizon is extended to the $(k+2)$th sample and (21) is rewritten as

$$\overline{\nu_s^*}(k+2) = R_\sigma \left\{ \frac{T_s + \tau_\sigma}{T_s} \left(\overline{i_s^*}(k+2) - \left(\frac{T_s + \tau_\sigma}{T_s} \right) \bar{i}_s^p(k+1) \right) \right\} - \left(\frac{k_r}{\tau_r} - j k_r \omega_m \right) \overline{\psi_r}(k) \tag{22}$$

Unlike the conventional PCC, wherein the optimal vector is identified with a current-based cost function, the proposed PCC

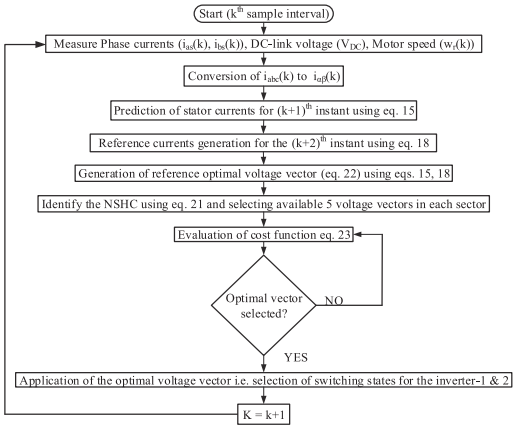

Fig. 5. Flow chart for the proposed PCC strategy.

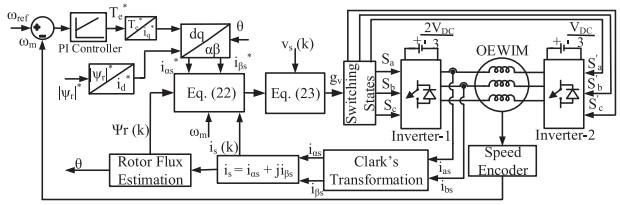

Fig. 6. Block diagram of proposed PCC for a 4-L OEWIMD.

employs a voltage-based cost function which is defined as

$$g_v(p) = \sqrt{\left|v^*_{\alpha s}(k+2) - v_{\alpha s}(k)_p\right|^2 + \left|v^*_{\beta s}(k+2) - v_{\beta s}(k)_p\right|^2} \quad (23)$$

where

$$p \in 0, 1, 2, 3, \text{ and } 4.$$

From (22), the reference voltage is generated. Similarly, based on the NSHC, the corresponding candidate VVs $(\bar{v}_s(k))$ in each sector are identified. Each of these five candidate vectors are individually tried out in (23) and the one which results in minimum error is identified as the optimal vector.

The detailed control algorithm flow chart and the block diagram to implement the proposed PCC technique for the 4-L OEWIMD are shown in Figs. 5 and 6, respectively.

Based on the above discussion, the following conclusions may be drawn: 1) The number of candidate states is reduced from 37 to 5, implying that the burden on the controller is reduced. 2) The switching frequency is also reduced as one of the inverter acts as the clamping inverter.

VI. Simulation and Experimental Results

The conventional PCC and the proposed PCC are simulated for a 3.7 KW, 1445 r/min, 400 V (Line-Line), 4-pole, 50 Hz OEWIMD supplied from two two-level VSIs. To achieve 4-L inversion, the dc-link voltages are maintained in the ratio of 2:1. The total dc-link voltage of the dual-inverter system is chosen as 564 V, i.e., inverter-1 is operated with 376 V, whereas inverter-2 is operated with 188 V. The OEWIMD parameters are tabulated in Table I. The MATLAB software is used to carry out the simulation.

TABLE I
OEWIMD Parameters

Stator resistance (R_s)	4.5 Ω
Stator inductance (L_s)	0.5632 H
Rotor resistance (R_r)	6.2 Ω
Rotor inductance (L_r)	0.5632 H
Magnetizing inductance (L_m)	0.54 H
Reference rotor flux (λ^*_r)	1.36 Wb

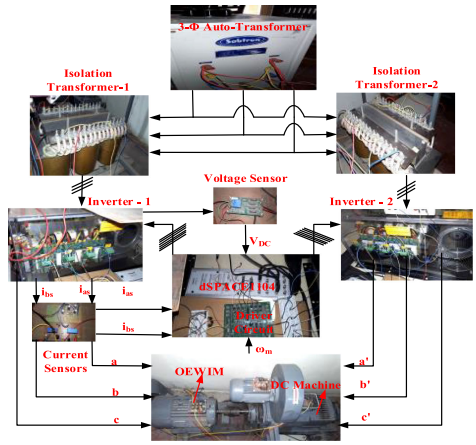

Fig. 7. Experimental set-up for 4-L OEWIMD.

To validate the simulation results, the experimental results are performed on OEWIMD (see Table I for motor parameters). The set-up used for the experimentation is shown in Fig. 7. The total dc-link voltage of the dual-inverter system is taken as 564 V to ensure rated motor phase voltage (i.e., 230 V). The Semikron IGBTs (1200 V, 30 A) are used in the dual-inverter system. The rapid prototyping dSPACE-1104 controller is used to implement the proposed PCC and generate the gating signals. Electrical isolation between the power circuit and the control platform is obtained with the optocoupler-based A3120 driver IC. One (1 number) hall-effect-based voltage sensor (LV 25-P) and two current sensors (LA 55-P) are used to sense the dc-link voltage of the dual-inverter system and the phase currents i_{as}, i_{bs} of the OEWIMD, respectively. The sampling time period for the experimentation is chosen as 120 μS.

When the OEWIMD is operated at low speeds (400 r/min), the tip of the reference VV is situated in the region of core-hexagon ABCDEF (Fig. 4). Under this condition, the conventional PCC evaluates all of the available candidate VVs to choose the optimal vector. In contrast, in the proposed PCC, inverter-1 is clamped to a null state (i.e., either 7 $(+++)$ or 8 $(---)$, providing a switched neutral point on one side), while inverter-2 is switched. Thus, at low speeds, with the proposed PCC, the 4-L OEWIMD is operated as the conventional two-level VSI driven induction motor drive.

The simulated and the experimentally obtained motor phase voltage $(v_{aa'})$ and current $(i_{aa'})$ waveforms for both of the methods at a speed of 400 r/min are shown in Figs. 8 and 9, respectively.

To demonstrate the principle of the proposed PCC technique, the experimentally obtained pole voltage of inverter-1 and inverter-2 is shown in Fig. 10, at a speed of 1200 r/min. From Fig. 10, it can be observed that both of the inverters are switched for the conventional PCC, whereas in the proposed PCC, inveter-2 is clamped to the switching state based on the

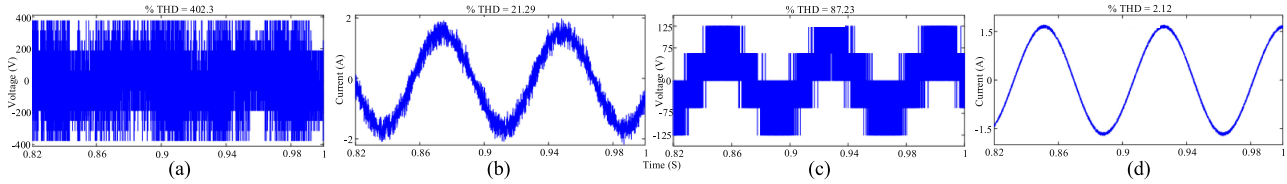

Fig. 8. Simulation results of (a) and (c) OEWIM $v_{aa'}$ and (b) and (d) $i_{aa'}$ at a speed of 400 r/min with (a) and (b) conventional PCC and (c) and (d) proposed PCC.

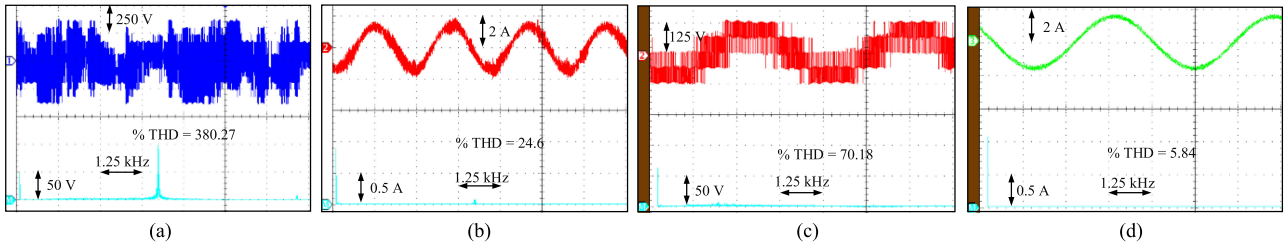

Fig. 9. Experimentally obtained (a) and (c) OEWIM $v_{aa'}$ and its harmonic spectrum [bottom trace of (a) and (c)], (b) and (d) $i_{aa'}$ and its FFT analysis [bottom trace of (b) and (d)] with (a) and (b) conventional PCC and (c) and (d) proposed PCC at a speed of 400 r/min. Scale: *X*-axis: (a) and (b) 40 ms/div, (c) and (d) 20 ms/div.

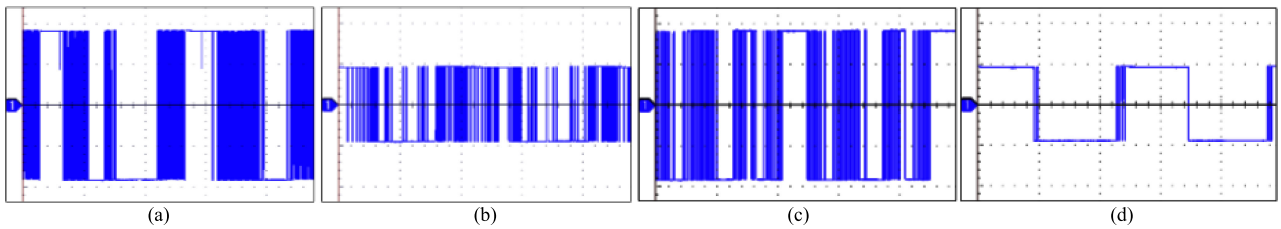

Fig. 10. Experimentally obtained pole voltage of (a) and (c) inverter-1 and (b) and (d) inverter-2 of the dual-inverter fed OEWIM. (a) and (b) Conventional PCC. (c) and (d) Proposed PCC. Scale: *X*-axis:10 ms/div, *Y*-axis: 100 V/div.

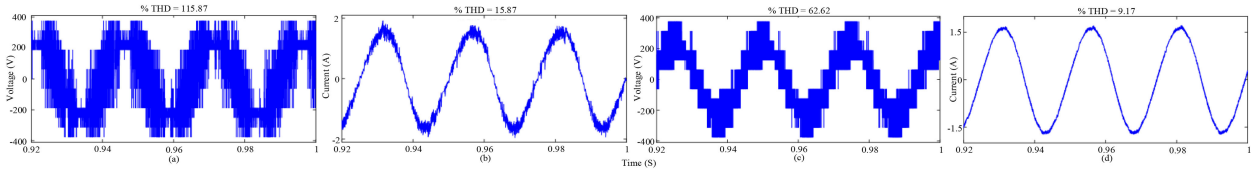

Fig. 11. Simulation results of (a) and (c) $v_{aa'}$ and (b) and (d) $i_{aa'}$ at a speed of 1200 r/min of OEWIM with (a) and (b) conventional PCC and (c) and (d) proposed PCC.

NSHC (see Fig. 4) and inverter-1 acts as switching inverter. It can be concluded that with the proposed PCC, there is a reduction in switching power loss at higher speeds.

The simulation and experimental results for the motor phase voltage and current are presented in Figs. 11 and 12, respectively, when the 4-L OEWIMD is operated at a speed of 1200 r/min.

From the simulation and the experimental results, it is evident that the proposed PCC results in a better performance with reduced voltage and current THDs, when compared to the conventional PCC.

The experimentally obtained steady-state electromagnetic torque of the OEWIMD for the FOC, conventional PCC, and proposed PCC is shown in Fig. 13, when it is operated at a speed of 1200 r/min. It is evident from Fig. 13 that the torque ripple is reduced with the proposed PCC, compared to the FOC and conventional PCC.

Fig. 14 presents the magnitudes of the cost function, (i.e., $|g|$) for the conventional and the proposed PCC, when the 4-L OEWIMD is operated at a speed of 1200 r/min. It may be noted that, unlike the conventional PCC, which uses 37 VVs, the proposed PCC uses only four vectors to obtain the optimal VV, which minimizes the error between reference and the predicted values of the motor phase current. From this, it can be intuitively reasoned out that in the proposed PCC, the burden on the controller is reduced as compared to the conventional PCC.

The average execution time for the conventional PCC and proposed PCC is shown in Table II. From Table II, the execution time spent for the prediction and optimization of proposed PCC is 22.7 μS and 50.14 μS for the conventional PCC. The burden on the controller is reduced by around 53% with the proposed PCC as compared to the conventional PCC.

The experimentally obtained motor phase current and its FFT analysis, torque, and the speed of the OEWIMD for the FOC, conventional PCC, and proposed PCC at a low speed of 90 r/min are shown in Fig. 15.

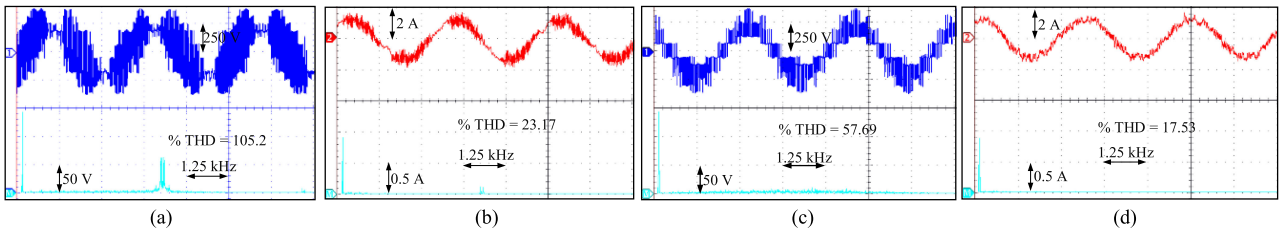

Fig. 12. Experimental results of (a) and (c) OEWIM $v_{aa'}$ and (b) and (d) $i_{aa'}$ with their FFT analysis [bottom trace of (a), (b), (c), and (d)] at a speed of 1200 r/min with conventional PCC (a, b) and proposed PCC (c, d). Scale: *X*-axis:10 ms/div.

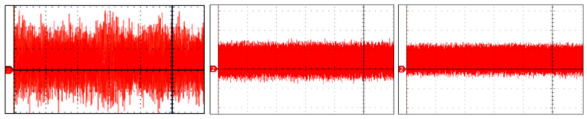

Fig. 13. Experimentally obtained steady-state torque of OEWIM at a speed of 1200 r/min with FOC (left), conventional PCC (middle), and proposed PCC (right). Scale: *X*-axis: 2 S/div, Y-axis: 3 N·m/div.

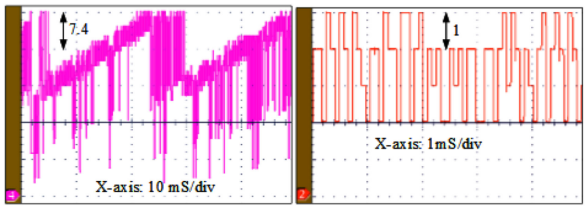

Fig. 14. Experimental cost function value of conventional PCC (left) and proposed PCC (right) at a OEWIM reference speed of 1200 r/min.

TABLE II
COMPUTATIONAL BURDEN ON THE CONTROLLER WITH SAMPLING TIME (Ts = 120 μS)

Name of the index	Execution Time (μS)	
	Conventional PCC	Proposed PCC
Measurements	11.92	
Rotor flux estimation	14.64	
PI-control & reference generation	14.56	
Prediction and optimization	50.14	22.7
Total	91.26	63.82

From Fig. 15, it can be observed that the performance of the proposed PCC is better in terms current THD and torque ripple as compared to both FOC and conventional PCC.

The dynamic performance of FOC technique and for both of the PCC techniques is assessed during acceleration, during speed reversal and for torque transient of the 4-L OEWIMD. The experimentally obtained waveforms during the acceleration of OEWIMD are shown in Fig. 16. From results it can be observed that the proposed PCC performs on par to the FOC and the conventional PCC, despite the lack of dedicated current controllers (compared to FOC) and restricted search for optimality (37 versus 5 vectors).

A speed reversal operation is performed at a speed of $\pm$ 1000 r/min without any load torque to investigate the speed transient response of the controller. The experimentally obtained waveforms are shown in Fig. 17.

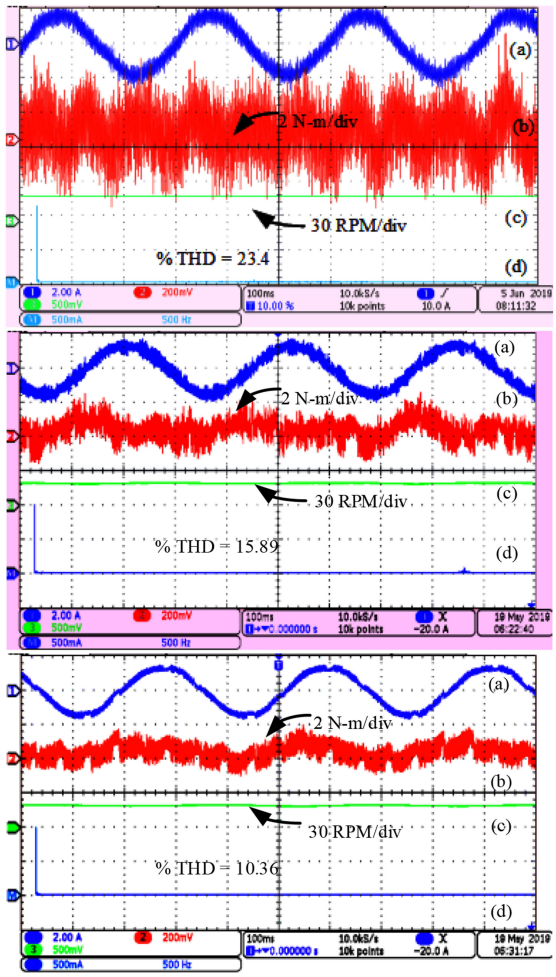

Fig. 15. Experimental results of OEWIMD running at a speed of 90 r/min with FOC (top), conventional PCC (middle), and the proposed PCC (bottom) techniques. (a) Phase current. (b) Torque. (c) Speed. (d) FFT analysis of phase current.

The torque transient response is demonstrated by applying a sudden load of 5 N·m with help of dc-generator connected to the shaft of the OEWIMD. The corresponding experimental results are shown in Fig. 18. From Fig. 18, it can be observed that for the same values of PI controller, the dynamic response of the proposed PCC technique is considerably quicker compared to the conventional PCC.

The total losses of the OEWIMD system consist of the power losses in the dual-inverter system and motor. The power loss in the dual-inverter system comprises of the sum of the switching

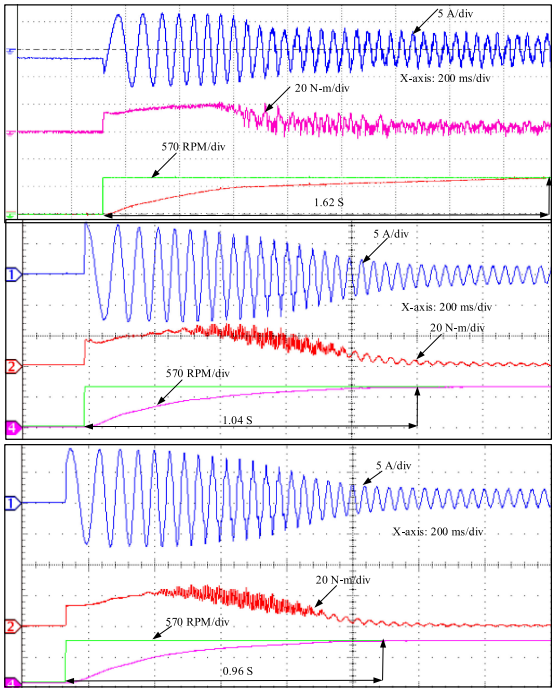

Fig. 16. Experimentally obtained stator current (first trace), torque (second trace), and speed (third and fourth traces) waveforms of OEWIM during acceleration: FOC (top), conventional PCC (middle), and proposed PCC (bottom).

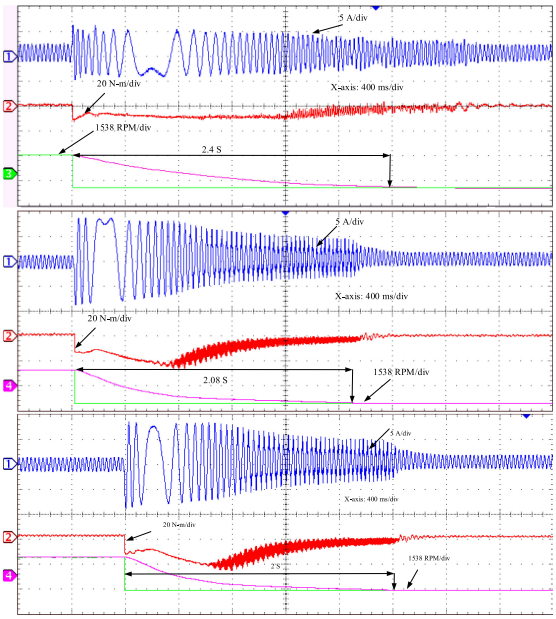

Fig. 17. Experimentally obtained stator current (first trace), torque (second trace), and speed (third and fourth traces) of OEWIMD during speed-reversal: FOC (top), conventional PCC (middle), and proposed PCC (bottom).

power loss and conduction loss of the power semiconductor switching devices. Further, the ripple in the motor current contributes to the ohmic loss in the motor. All of these losses are evaluated by employing the *loss model,* which was suggested for 4-L OEWIMD [27].

In order to make a fair comparison in computation of device losses, the total dc-link voltage is kept at 564 V and the load on the OEWIMD is considered as 80% (i.e., 20 N·m, see Table I).

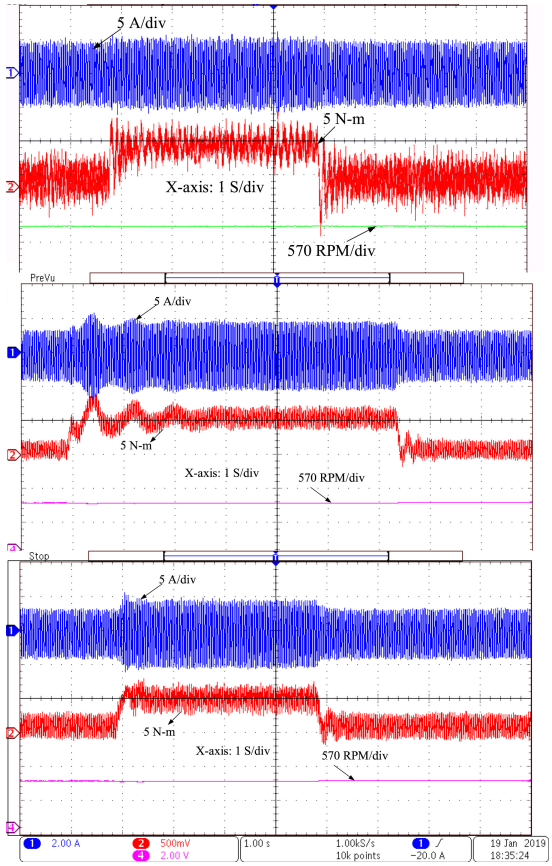

Fig. 18. Experimentally obtained stator current (first trace), torque (second trace), and speed (third trace), when sudden load was applied on the OEWIMD: FOC (top), conventional PCC (middle), and proposed PCC (bottom).

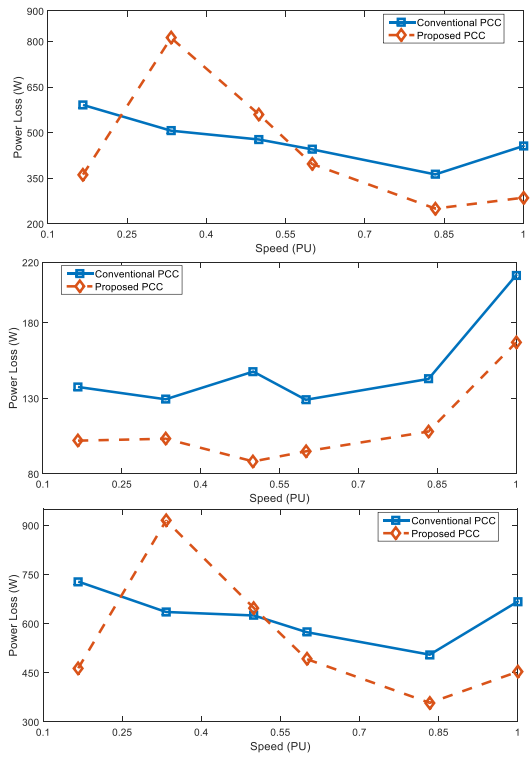

Fig. 19. Total power loss of 4-L OEWIMD: dual-inverter loss (top), ohmic loss (middle), and drive loss (bottom).

Fig. 19 presents the total power loss incurred in the dual-inverter fed 4-L OEWIMD. From Fig. 19, it can be observed that, owing to the randomness associated with the control strategy in terms of the choice of switching vectors, which results in variable switching operation, no definitive statement can be made regarding the trends in the switching power loss (which dominates the power loss in the dual-inverter system) in general. However, for the present system, the control strategy results in the switching of only inverter-2 in the low-speed range, while inverter-1 is clamped. Similarly, in the high-speed range, inverter-2 is practically clamped, while inverter-1 is switched. This is the reason for the low power loss of the dual-inverter system in the low, as well as in the high-speed range. This trend is carried over to the overall drive loss also, as the power loss in the dual-inverter system is significantly higher, compared to the ohmic power loss in the OEWIM.

VII. Conclusion

This article proposes an improvised PCC for a 4-L OEWIMD. The conventional PCC for this drive evaluates 37 candidate VVs to select the optimal one, which increases the computational burden on the controller and results in a variable switching frequency. In contrast, the proposed PCC tests only five candidate vectors to determine the optimal VV. The proposed algorithm is based on the NSHC corresponding to the inverter with lower dc-link voltage and the clamping of that inverter. Thus, with the proposed PCC strategy, the burden on the controller is reduced. The simulated as well as the experimental results indicate that the proposed PCC technique results in a better performance in terms of the voltage THD, current THD, and the steady-state torque ripple. The switching frequency is also reduced with the proposed PCC as compared with the conventional PCC technique. This advantage manifests as the reduction of overall loss of the 4-L OEWIMD system for most of the operating speed range.

References

[1] Y. A. I. Mohamed and E. F. El-Saadany, "Robust high bandwidth discrete-time predictive current control with predictive internal model—A unified approach for voltage-source PWM converters," *IEEE Trans. Power Electron.*, vol. 23, no. 1, pp. 126–136, Jan. 2008.

[2] M. Narimani, B. Wu, V. Yaramasu, Z. Cheng, and N. R. Zargari, "Finite control-set model predictive control (FCS-MPC) of nested neutral point-clamped (NNPC) converter," *IEEE Trans. Power Electron.*, vol. 30, no. 12, pp. 7262–7269, Dec. 2015.

[3] R. Vargas, U. Ammann, B. Hudoffsky, J. Rodriguez, and P. Wheeler, "Predictive torque control of an induction machine fed by a matrix converter with reactive input power control," *IEEE Trans. Power Electron.*, vol. 25, no. 6, pp. 1426–1438, Jun. 2010.

[4] J. Rodriguez *et al.*, "Predictive current control of a voltage source inverter," *IEEE Trans. Ind. Electron.*, vol. 54, no. 1, pp. 495–503, Feb. 2007.

[5] S. Kouro, P. Cortes, R. Vargas, U. Ammann, and J. Rodriguez, "Model predictive control—A simple and powerful method to control power converters," *IEEE Trans. Ind. Electron.*, vol. 56, no. 6, pp. 1826–1838, Jun. 2009.

[6] J. Rodriguez and P. Cortes, *Predictive Control of Power Converters and Electrical Drives*. 1st ed. Hoboken, NJ, USA: Wiley, 2012.

[7] S. Vazquez *et al.*, "Model predictive control: A review of its applications in power electronics," *IEEE Ind. Electron. Mag.*, vol. 8, no. 1, pp. 16–31, Mar. 2014.

[8] P. Cortes, J. Rodriguez, C. Silva, and A. Flores, "Delay compensation in model predictive current control of a three-phase inverter," *IEEE Trans. Ind. Electron.*, vol. 59, no. 2, pp. 1323–1325, Feb. 2012.

[9] W. Xie, X. Wang, F. Wang, W. Xu, R. Kennel, and D. Gerling, "Dynamic loss minimization of finite control set-model predictive torque control for electric drive system," *IEEE Trans. Power Electron.*, vol. 31, no. 1, pp. 849–860, Jan. 2016.

[10] C. Xue, W. Song, X. Wu, and X. Feng, "A constant switching frequency finite-control-set predictive current control scheme of a five-phase inverter with duty-ratio optimization," *IEEE Trans. Power Electron.*, vol. 33, no. 4, pp. 3583–3594, Apr. 2018.

[11] S. Lakhimsetty, V. S. P. Satelli, R. S. Rathore, and V. T. Somasekhar, "Multilevel torque hysteresis-band based direct-torque control strategy for a three-level open-end winding induction motor drive for electric vehicle applications," *IEEE J. Emerg. Sel. Topi cs Power Electron.*, vol. 7, no. 3, pp. 1969–1981, Sep. 2019.

[12] F. Wang, X. Mei, P. Tao, R. Kennel, and J. Rodriguez, "Predictive field-oriented control for electric drives," *Chin. J. Electr. Eng.*, vol. 3, no. 1, pp. 73–78, Jun. 2017.

[13] S. Sajadian and R. Ahmadi, "Model predictive control of dual-mode operations z-source inverter: Islanded and grid-connected," *IEEE Trans. Power Electron.*, vol. 33, no. 5, pp. 4488–4497, May 2018.

[14] P. Karamanakos, P. Stolze, R. M. Kennel, S. Manias, and H. du Toit Mouton, "Variable switching point predictive torque control of induction machines," *IEEE J. Emerg. Sel. Topics Power Electron.* vol. 2, no. 2, pp. 285–295, Jun. 2014.

[15] R. O. Ramírez, J. R. Espinoza, F. Villarroel, E. Maurelia, and M. E. Reyes, "A novel hybrid finite control set model predictive control scheme with reduced switching," *IEEE Trans. Ind. Electron* ., vol. 61, no. 11, pp. 5912–5920, Nov. 2014.

[16] H. Abu-Rub, J. Guziński, J. Rodriguez, R. Kennel, and P. Cortés, "Predictive current controller for sensorless induction motor drive," in *Proc. IEEE Int. Conf. Ind. Tech nol* ., Vina del Mar, Chile, 2010, pp. 1845–1850.

[17] B. Zhu, K. Rajashekara, and H. Kubo, "Comparison between current-based and flux/torque-based model predictive control methods for open-end winding induction motor drives," *IET Electric Power Appl*., vol. 11, no. 8, pp. 1397–1406, Sep. 2017.

[18] S. Odhano, R. Bojoi, A. Formentini, P. Zanchetta, and A. Tenconi, "Direct flux and current vector control for induction motor drives using model predictive control theory," *IET Electric Power Appl.*, vol. 11, no. 8, pp. 1483–1491, Sep. 2017.

[19] Y. Xue *et al.*, "Vector-based model predictive hysteresis current control for asynchronous motor," *IEEE Trans. Ind. Electron.*, vol. 66, no. 11, pp. 8703–8712, Nov. 2019.

[20] P. Acuna, C. A. Rojas, R. Baidya, R. P. Aguilera, and J. E. Fletcher, "On the impact of transients on multistep model predictive control for medium-voltage drives," *IEEE Trans. Power Electron.*, vol. 34, no. 9, pp. 8342–8355, Sep. 2019.

[21] Z. Huang *et al.*, "Voltage utilization enhancement of dual inverters by model predictive control for motor drive applications," in *Proc. IEEE Int. Symp. Predictive Control Electr . Drives Power Electron.*, Quanzhou, China, 2019, pp. 1–3.

[22] M. S. Mousavi, S. A. Davari, C. Garcia, J. Rodriguez, and F. Wang, "Cascaded finite control-set model predictive control for the dual inverter fed open-end winding induction motor with four-level inversion," in *Proc. IEEE Int. Symp. Predictive Control Electr . Drives Power Electron.*, Quanzhou, China, 2019, pp. 1–6.

[23] B. V. Reddy and V. T. Somasekhar, "A dual inverter fed four-level open-end winding induction motor drive with a nested rectifier-inverter," *IEEE Trans. Ind. Informat.*, vol. 9, no. 2, pp. 938–946, May 2013.

[24] V. T. Somasekhar, K. Gopakumar, M. R. Baiju, K. K. Mohapatra, and L. Umanand, "A multilevel inverter system for an induction motor with open-end windings," *IEEE Trans. Ind. Electron.*, vol. 52, no. 3, pp. 824–836, Jun. 2005.

[25] M. B. Patil, V. Ramanarayanan, and V. T. Ranganathan, *Simulation of Power Electronic Circuits*. 1st ed., Oxford, U.K.: Alpha Science Int., 2009.

[26] S. Lakhimsetty, N. Surulivel, and V. T. Somasekhar, "Improvised SVPWM Strategies for an enhanced performance for a four-level open-end winding induction motor drive," *IEEE Trans. Ind. Electron.*, vol. 64, no. 4, pp. 2750–2759, Apr. 2017.

[27] S. Lakhimsetty and V. T. Somasekhar, "A four-level open-end winding induction motor drive with a nested rectifier–inverter combination with two DC power supplies," *IEEE Trans. Power Electron.*, vol. 34, no. 9, pp. 8894–8904, Sep. 2019.